Universidad
Carlos III de Madrid

e-Archivo

Institutional Repository

This is a postprint version of the following published document:

González, M.; Baselga, J.; Pozuelo, J. (2016). "High porosity scaffold composites of graphene and carbon nanotubes as microwave absorbing materials". *Journal of Materials Chemistry C*, Issue 36, pp. 8575-8582. https://doi.org/10.1039/C6TC01984F

High porosity scaffold composites of graphene and carbon nanotubes as microwave absorbing materials†

M. González, J. Baselga and J. Pozuelo*

The design of microwave absorbing materials requires low reflection and high absorption of radiation simultaneously. Low reflection of electromagnetic waves can be achieved inducing porous faces which minimize the impedance mismatch. High absorption can be obtained by increasing the conductivity of the material. We report the preparation of highly porous scaffolds from a combination of graphene and carbon nanotubes. The bimodal porous structure was controlled making use of the surface properties of graphene oxide that are able to stabilize hexane droplets in aqueous dispersions of graphene oxide and carbon nanotubes. After hydrothermal and two step freeze-drying processes, macro- (220 microns) and mesoporous (10 microns) structures, due to hexane droplets and freeze drying, respectively, were obtained. DC conductivities of 8.2, 14.7, 33.2, and 60.7 S m^{-1} were obtained for graphene scaffolds containing 0, 10, 20 and 40% of carbon nanotubes respectively. An electromagnetic characterization was performed on scaffolds infiltrated with epoxy resin; using appropriate models, the electromagnetic properties of the conducting phase have been obtained. Scaffolds with a thickness of 9 mm were able to absorb up to 80% of the incident radiation keeping the reflection as low as 20%.

Introduction

There is a current strong interest in the development of microwave absorbers and shielding materials due to the increasing environmental electromagnetic pollution.[1,2] There are three possible interactions of electromagnetic waves with matter. When the wave reaches the front-face of the material, part of the incident power is reflected and the non-reflected power is transmitted through the sample; the transmitted portion can be absorbed or transmitted out from the slab. Partial reflection occurs when the incident electromagnetic wave propagating through a medium with impedance Z_0 reaches the surface of a material with a different impedance value Z_M. The reflected power depends on the impedance mismatch and falls to zero when $Z_M = Z_0$.[3] The absorbed power also depends on the impedance of the material, that is, both the reflection and absorption processes are favoured in materials with high

conductivity. However, if the reflection losses are high, only a small portion of the radiation is able to penetrate into the material and therefore the material will not behave as an efficient absorber. Porous conductive materials decrease the impedance mismatch between the medium and the material, and are, therefore, alternatives for the preparation of microwave absorbers.

In a previous report[4] we prepared porous CNT scaffolds from aqueous CNT dispersions using chitosan as an organic binder. Power analysis revealed particularly low transmitted power (less than 10%) and high absorbed power (close to 70%). More interestingly, samples with the highest pore size and porosity presented the lowest and highest reflected and absorbed power respectively. The presence of a dielectric (chitosan) at the CNT interfaces limited both the conductivity and absorption behaviour at low frequencies (below 8 GHz). In this paper, we present novel porous structures in which chitosan is substituted by graphene which acts as the CNT binder and as a surfactant controlling the pore size and stabilizing the scaffold's structure.

Graphene oxide (GO) is formed by oxidized graphene amphiphilic fragments which present a random distribution of aliphatic and aromatic regions.[5] GO possesses hydrophilicity due to the presence of oxidized aliphatic regions containing tetrahedral sp^3 carbon atoms, whereas hydrophobicity is due to the presence of aromatic regions with benzene rings containing planar sp^2 carbon atoms.[6] It contains numerous functional groups mainly epoxy and

Departamento de Ciencia e Ingeniería de Materiales e Ingeniería Química (IAAB), Universidad Carlos III de Madrid, 28911 Leganés, Madrid, Spain.
E mail: jpozue@ing.uc3m.es; Fax: +34 91 6249430

hydroxyl groups on the plane, whereas carboxyl, carbonyl, ester, ether, diol, ketone, phenol, quinine and lactone groups are present at the edge surfaces of the GO sheets.[7] The oxidized functionalities present on the basal and edge planes render it suitable for the high dispersion in aqueous solutions and pave the way for the chemical functionalization,[5] such as amidation at the carboxylic groups[8] or nucleophilic substitution *via* epoxy groups.[9] On the other hand, the aromatic regions having sp[2] networks provide active sites to interact with other aromatic molecules through π–π supramolecular interactions.[10]

Self-assembly and reduction of GO into interconnected graphene networks are simultaneously achieved by heat treating aqueous GO suspensions for a certain amount of time inside a Teflon-lined autoclave.[11,12] During the hydrothermal process, the oxygen contained in the functional groups of GO is gradually eliminated, and the conjugated structures are restored. The increasing hydrophobicity and π–π interactions between reduced graphene cause a random self-assembly of the flexible sheets in 3D-hydrogels with pore size distribution ranging from sub-micrometres to a few micrometres.[13,14]

In addition, it has been proved that GO is a good CNT dispersant forming stable dispersions of CNTs; the resulting dispersion is a novel hybrid named graphene oxide–CNTs (GO–CNTs).[15] Some studies have also proved that GO–CNT and graphene–CNT hybrid nanomaterials exhibit higher electrical conductivities, large specific areas and catalytic properties compared with either pristine CNTs or GO/graphene.[16,17] If an amount of oxidized CNTs is added to GO dispersions, monoliths obtained after the hydrothermal process are formed by both compounds. The strong π–π stacking interaction existing between graphene planar fragments and between graphene and CNTs provides an exceptional stability to the 3D network of the resulting hybrid material.[18]

To control the pore size and to obtain hierarchical pore morphology we have modified an already reported hydrothermal method[19] which involves the preparation of stable aqueous emulsions of graphene oxide containing hexane droplets. A subsequent careful cold evaporation of hexane followed by lyophilisation of the aqueous phase allows us to achieve more consistent scaffold structures and displaces and compresses the CNT–rGO towards the walls of the ice crystal structure increasing the CNT connectivity and, consequently, the conductivity of the material.

Experimental

Materials

Graphite powder (with a purity > 99.999%) was purchased from Alfa Aesar. Multi-walled carbon nanotubes Graphistrength® C100 (with a purity > 90%) were purchased from Arkema Inc. Hexane (Panreac) was used as an organic phase. The hydrogenated derivative of diglycidyl ether of bisphenol-A (HDGEBA) epoxy resin was supplied by CVC Specialty Chemicals (USA); its epoxy equivalent mass was 210 g mol^{−1} determined by acid titration. *m*-Xylylenediamine (Sigma-Aldrich) was used as a curing agent. H_2O_2 30% w/v (Panreac), $KMnO_4$ (Panreac),

$NaNO_3$ (Sigma-Aldrich) and H_2SO_4 98% v/v (Panreac) were employed for graphite and CNT oxidation and used without any further purification.

Hybrid composites preparation

GO was prepared by a modified Hummer's method.[20] In a typical experiment a 500 mL flask equipped with a thermometer and cooled in an ice-water bath was fed with 4 g of graphite and 2 g of $NaNO_3$; 180 mL of concentrated H_2SO_4 was added to the flask and stirred for 2 hours. Then, 11 g of $KMnO_4$ were added slowly to the mixture. The rate of addition was carefully controlled to keep the reaction temperature below 20 °C. After adding the oxidant, the ice-water bath was removed and stirring was continued for 2 hours at room temperature. The oxidation process was stopped adding very slowly 180 mL of H_2O. As the reaction temperature rapidly increased to 80 °C, 30 mL of 30% H_2O_2 were added to the mixture. For purification, the mixture was washed by rinsing with distilled water and centrifuged at 4500 rpm for 30 min several times until the pH of the solution was 6–7. After freeze-drying, GO was obtained as a solid.

To remove the extreme CNT hydrophobicity while keeping their aspect ratio, oxidation with H_2O_2/UV was performed.[21] In a typical experiment, 100 mL of H_2O_2 (30% wt) was added to 1 g of CNT keeping the mixture in an ultrasonic bath for three minutes; then the mixture was exposed to UV light (Philips Lighting 250HPLN 250W) for 15 minutes stirring with a magnetic stirrer. The dispersion was filtered and washed three times with distilled water and finally dried under vacuum. Scaffolds were prepared by a modified hydrothermal reduction method reported by Li *et al.*[19]

Fig. 1 shows a schematic illustration of the synthetic process. Aqueous dispersions of GO:CNT were prepared with a total concentration of carbonaceous nanoparticles of 5 mg mL^{−1}, varying the proportion of CNTs from 0 to 40%. In a typical experiment, 8 mL of an aqueous dispersion was mixed with 4 mL of hexane and shaken vigorously to form a homogeneous emulsion. The emulsion was sealed in a 20 mL Teflon autoclave and maintained at 180 °C for 10 h; afterwards the autoclave was naturally cooled to room temperature and the hexane containing gel was removed. Attempts to remove hexane solvent *via* the hot water treatment[19] were not successful because of the collapse of
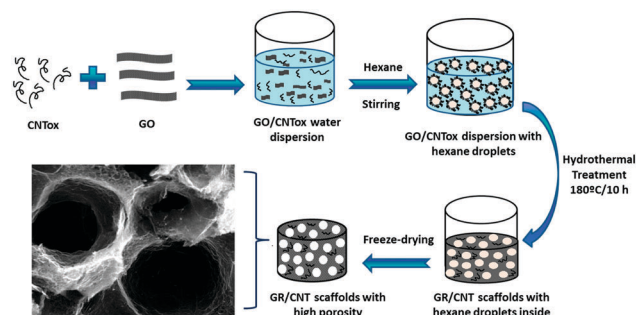

Fig. 1 Schematic illustration of the synthetic process of a GR:CNT hybrid scaffold with high porosity.

the macropores. Alternatively, we found that a previous hexane cold evaporation under vacuum with the scaffold, frozen at 10 °C, was a successful approach. After hexane was completely removed freeze-drying of the frozen hexane-free scaffold was performed to avoid serious volume shrinkage during the process of water removal and to preserve the shape and porous 3D structure.[22]

Techniques

GO, GR, CNTs and GR:CNTs were characterized by Wide-Angle X-Ray Diffraction (XRD, Panalytical X'pert Pro X-ray diffractometer with Cu Kα radiation, $\lambda = 0.15406$ nm). SEM images were obtained using a Philips XL 30 scanning electron microscope. X-ray photoelectron spectroscopy (XPS) was carried out using an ESCAPROBE P equipped with a monochromatized Mg X-ray source (1253.6 eV photons) and a hemispherical analyser Omicron EA125 to analyse the chemical composition of the composites. Raman spectroscopy was carried out using an inVia confocal Raman microscope (Renishaw) using the 514.5 nm laser excitation. For each sample, various spectra were recorded in different places in order to verify the homogeneity of the sample. Thermogravimetric analysis (TGA) was carried out using a simultaneous thermal analyser Perkin Elmer 6000STA under an air atmosphere from room temperature to 1000 °C at 10 °C min^{-1}. Differential scanning calorimetry (Mettler Toledo DSC 822e) was used to measure the T_g of the epoxy resin. The electrical properties of the composites were evaluated using a HP 34401A source meter with 100 μΩ resolution. Measurements were performed in 4-wire DC configuration to obviate the electrical resistance of the wires. The temperature of the samples during the measurement was 25 °C.

The global electromagnetic shielding efficiency, SE_T, can be quantified as the sum of the contributions of reflection and absorption mechanisms. For these purposes, the scattering parameters S_{11} and S_{21} were determined using a vector network analyzer (Agilent, ENA, E5071) equipped with a 7 mm coaxial transmission line adapter in the range of 1 to 18 GHz. An ENA instrument measures both the transmitted and reflected power coefficients ($T = |S_{21}|^2 = |S_{12}|^2$ and $R = |S_{11}|^2 = |S_{22}|^2$), therefore the absorbed power coefficient of the material (A) is:

$$A = 1 \quad (R + T) \quad (1)$$

The ratios between the scattering parameters and the transmission, reflection and absorption EMI shielding effectiveness are given by the following equations.

$$SE_T = \quad 10 \log(T) = \quad 10 \log(|S_{21}|^2) \quad (2)$$

$$SE_R = \quad 10 \log(1 \quad R) = \quad 10 \log(1 \quad |S_{11}|^2) \quad (3)$$

$$SE_A = \quad 10 \log\left(\frac{T}{1 \quad R}\right) = \quad 10 \log\left(\frac{|S_{21}|^2}{1 \quad |S_{11}|^2}\right) \quad (4)$$

The scattering parameters were also used to calculate the complex magnetic permeability and dielectric permittivity of the hybrid composites. The measurements were performed according to the transmission/reflection method.[23] For electromagnetic characterization, the scaffolds were vacuum infiltrated with an epoxy resin, as described previously,[24] cured and machined to the final required geometry for the coaxial line: rectangular

toroids of nominal internal and external diameters close to 3.04 and 7 mm respectively. Using the built-in software, a geometry correction was applied for small deviations from nominal geometry.[23]

Results and discussion

Scaffold characterization

Interfacial tension in the water/n-hexane system is rather high (~ 51 mN m^{-1}) and their mixtures quickly demulsify when stirring is stopped.[25] However, in the presence of GO, the suspensions remain stable for long periods of time (>6 months). As already mentioned, the partially disrupted 2D sp^2 lattice characteristic of GO sheets contains oxidized functionalities mainly at their edges[20] which confer amphiphilic properties to the sheets. GO therefore adsorbs on the surface of hexane droplets and other nonpolar solvents acting as an emulsion stabilizer and preventing their breakdown and coalescence from water suspensions.[7,26] This effect also remains when GO is partially substituted by CNTs with a droplet mean size of 212 microns (see the ESI†).

During the hydrothermal process the graphene oxide sheets are reduced and assembled around the hexane droplets which act as soft templates for macroporous structures.[19] The hybrid aerogels exhibit a three-dimensional network structure composed of hierarchical distribution of pores. SEM images shown in Fig. 2 reveal big pores with a diameter of 220 ± 40 microns irrespective of the CNT content (see the ESI†). These pores are embedded in the aerogel matrix and their walls are composed of randomly oriented CNTs, wrinkled graphene sheets and a lot of micropores with a mean diameter of 5 ± 1.5 microns enclosed by CNTs and graphene sheets. The macropores are formed by the collapse of
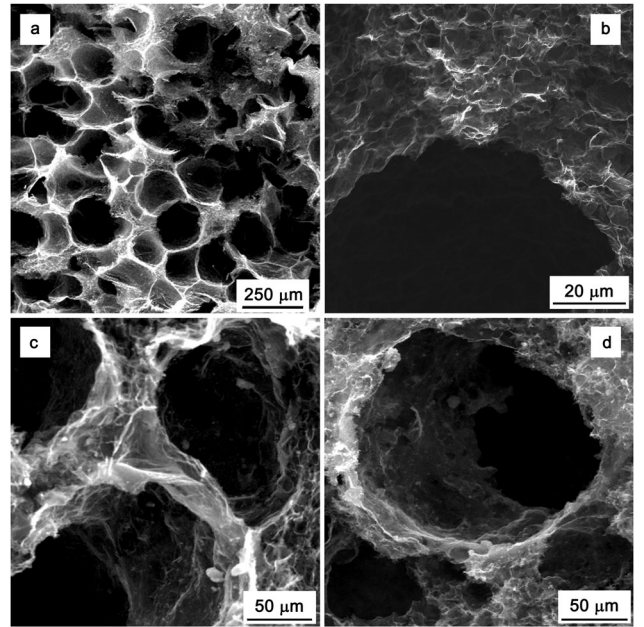

Fig. 2 SEM images of hierarchical distribution of pore sizes: macropores formed around the n hexane soft template drops (a and b). GR, (c) GR:CNT10%, and (d) GR:CNT40%.

the carbonaceous constituents around the *n*-hexane soft template droplets and the micropores, as already reported, are attributed to water exclusion due to the collapse of graphene sheets during the hydrothermal process.[13] It is worth noting that the macropore size do not experience any substantial change during the hydrothermal process.

XRD patterns of the graphene and carbon nanotubes before and after the hydrothermal treatment are shown in Fig. 2SI (ESI†). The typical diffraction peak for GO before dispersion appears at around 12° while after hydrothermal treatment it shifts to 23.78°, indicative of graphitic structures. Nevertheless, the *d*-spacing in the aerogel (0.382 nm) is still slightly larger than in the well-ordered graphite (0.335 nm).[27] These results suggest the partial reduction of GO in the hydrothermal reduction and the existence of π–π stacking between graphene sheets after hydrothermal treatment.[26]

The XRD pattern of oxidized carbon nanotubes (CNTox) shows two intense peaks at scattering angles of 26.1° and 44.25° which correspond to (0 0 2) and (1 0 1) planes of hexagonal graphite respectively. Some other low intensity peaks corresponding to the remaining catalyst iron oxides can also be observed. Hydrothermal treatment does not affect the structure and composition of the CNTs showing a similar interlayer spacing of 0.413 nm.

The reduction process of GO and CNTox was evaluated by X-ray photoelectron spectroscopy (XPS). Fig. 3 and Table 1 reveal that: (a) the hydrothermal treatment of graphene involves a significant decrease of the C–O signal, confirming that most of the epoxide and hydroxyl groups were successfully removed; (b) unsaturated and aliphatic carbon almost doubles its amount; (c) the amount of oxygen is reduced to about half its initial value. These results confirm that the supercritical water produced under the hydrothermal condition plays the role of a reducing agent and offers an effective reduction approach for graphene oxide.[26] By contrast, oxidized carbon nanotubes show no significant changes after HT.

GO and GR were characterized by FTIR (ESI†). FTIR spectra show absorption peaks at 3430 cm^{-1} (the O–H stretching mode), 1726 cm^{-1} (the C O stretching mode), 1629 cm^{-1} (the C C stretching mode), 1365 cm^{-1} (the C–OH stretching mode) and 1054 cm^{-1} (the C–O stretching mode).[28] After the hydrothermal treatment, the intensities of these absorption peaks decrease compared with those in the GO, indicating the restoration of a graphitic structure in graphene consistently with XRD and XPS results.

Raman spectra (ESI†) show the two characteristic D and G bands located at about 1350 and 1590 cm^{-1} respectively. The G peak occurs due to bond stretching of sp^2 C–C bonds whereas the D peak is due to breathing of sp^3 C–C bonds in six-atom rings and requires defects for its activation. Similar I_D/I_G ratios were obtained for CNTox and CNTs (∼1.20) and for GO and GR (1.0–1.1).

Electromagnetic characterization

The scaffolds were infiltrated with HDGEBA/*m*-xylylenediamine (see the ESI†) for electromagnetic characterization. Cured samples were machined to the final required geometry for the coaxial line: rectangular toroids of internal diameter of 3.04–3.05 mm and
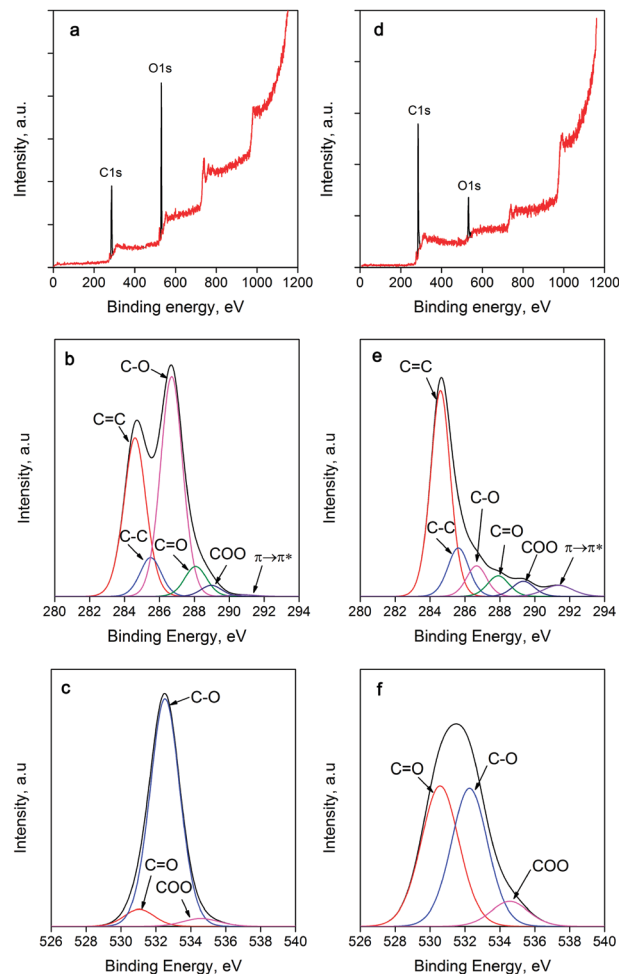

Fig. 3 XPS spectra of (a) GO and (d) GR. The C1s peak of GO (b) and GR (e). The O1s peak of GO (c) and GR (f).

Table 1 Compositional analysis by XPS

		GO	GR	CNTox	CNT
Carbon atoms, %	C═C	34.9	59.9	72.1	68.6
	C C	8.1	15.0	6.7	6.2
	C O	47.8	9.1	7.2	12.0
	C═O	6.5	6.5	5.1	4.8
	COO	2.3	4.9	3.5	3.4
	π → π*	0.4	4.7	5.4	5.0
	C^a	76.2	88.9	98.2	98.0
Oxygen atoms, %	C═O	6.8	47.2	62.7	79.3
	C O	89.4	44.5	33.2	17.5
	COO	3.8	8.3	4.2	3.2
	O^a	23.8	11.1	1.8	2.0

^{a} Global ratio of C and O atoms.

external diameter of 6.95–7.00 mm. To evaluate the epoxy curing, the glass transition temperatures were evaluated by DSC (ESI†). No differences in glass transition temperatures were observed between epoxy resin (77.6 °C) and scaffold composites; therefore the scaffold does not affect the curing of the epoxy resin.

Although it is not precisely known how GR sheets are bonded during the hydrothermal treatment,[19] it is accepted

that the sheets are located around the template droplets in a 2D fashion and packed in a thicker section as water is expelled. At the same time, although graphene becomes reduced, as already shown, the perfect hexagonal "graphene" framework cannot be completely recovered due to the existence of residual groups, defects and edges; therefore, the conductivity of GR should be lower than that of graphite.[29] Direct current conductivity, σ_{DC}, measurement of the GR scaffold (0% CNTs) yields a value of: 8.2 S m^{-1}. Assuming a value of 1.8 g cm^{-3} for the graphene density, the GR volume fraction in the scaffold is $\sim 10^{-2}$; assuming again an effective medium model for the conductivity of the scaffold, the true conductivity of the GR walls can be calculated as ~ 800 S m^{-1}. This value is between one and two orders of magnitude lower than reported conductivity data for graphite powders,[30] confirming thus that the graphene sp^2 framework has not been completely recovered.

DC conductivity data for scaffolds containing CNTs are 14.7, 33.2 and 60.7 S m^{-1} for 10, 20 and 40% CNTs respectively. These results are higher than for the only-graphene scaffold and indicate that the conductivity of composites increases with the CNT concentration probably due to the formation of more conductive CNT network paths and π–π interactions throughout the pore walls.

Permittivity will have the contribution of both epoxy and GR-CNTs, and hence, its value will be lower than that of a material exhibiting analogous conductivity values but being compact or non-porous.[31] These composites might exhibit low permittivities more similar to the epoxy resin than to a conductive material and will strongly depend on the volume fraction of the conductor phase.[32] It has been corroborated that the effective permittivity of aerogels, with almost all phase combinations, geometries and distributions, is less restrictive and depends on the volume fraction and the complex permittivity of each phase in the composite. The permittivity of composites with high epoxy fractions should be smaller than that of the conductive filler.[33]

Effective permittivity values are presented in Fig. 4, along with the measured permittivity of pure epoxy, in which the real part (ε') represents the charge storage and the imaginary part (ε'') is a measure of dielectric dissipation or losses. Both the real and imaginary parts decrease smoothly with frequency, a fact that is attributed to the Maxwell–Wagner polarization effect. This may arise from the reduction of the electric field induced in the porous composites in response to the reverse external electric field caused by the delay in the molecular polarization at higher frequency.[29] As can be seen, the real (ε') and imaginary (ε'') permittivities grow as the concentration of CNTs increases. These results are reasonable and can be attributed to the fact that the increasing content of CNTs increases the dipolar polarization and electrical conductivity.[35] In the case of ε' this is a direct consequence of a higher number of interfaces prompting polarization (Maxwell–Wagner–Sillars effect) associated with the migration and accumulation of charges at the conductive filler/polymer interfaces.[34] For ε'', it is due to the reduction of the average distance between adjacent CNTs which, in turn, implies higher dielectric and ohmic losses.
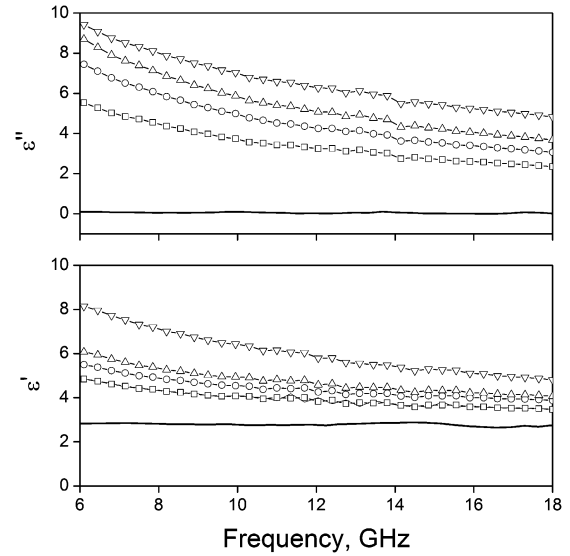

Fig. 4 Dielectric permittivity of epoxy (line), and effective dielectric permittivity of GR (□), GR:CNT10% (○), GR:CNT20% (△), and GR:CNT 40% (▽).

However, the measured permittivity data are effective values of a mixture of two very different phases. To extract relevant information of the conducting phase, which cannot be measured due to its porous nature, it is possible to make use of the effective medium theory and the Maxwell–Garnett equation which relates the properties of the ensemble with the properties of each phase. This model is based on the assumption that the structure of porous materials can be reasonably described as coated spheres and has been used to calculate effective permittivity of similar systems, i.e. silicon carbide foams[36,37] For an isotropic composite material consisting of two components (host and guest), the effective permittivity derived from the model Maxwell–Garnett model can be expressed as:

$$\varepsilon_{\text{eff}} = \varepsilon_1 \frac{(\varepsilon_2 + 2\varepsilon_1) + 2\phi_2(\varepsilon_2 \quad \varepsilon_1)}{(\varepsilon_2 + 2\varepsilon_1) \quad \phi_2(\varepsilon_2 \quad \varepsilon_1)} \quad (5)$$

where ε_1 and ε_2 are electric permittivities of the host (conductor phase) and the guest (epoxy phase) and ϕ_2 is the volume fraction of the epoxy.

From the results of effective permittivity of epoxy composites, real and complex permittivities of the conductive graphene and carbon nanotube walls have been estimated. Fig. 5 shows the calculated permittivity behaviour of this phase with frequency. It is possible to observe how the real part of the permittivity increases with the amount of carbon nanotubes mainly due to the increased interface extent between conductive fillers; additionally, values of the order of magnitude of graphite are obtained for the sample without nanotubes (GR).[38] This last result reflects the packing of GR platelets since the permittivity of a single graphene sheet is considerably lower, about 1.8–3.[39]

However, the most remarkable result is the high value of ε'' for all the studied systems. The complex part of the permittivity is an order of magnitude greater than the real part. This suggests that the mechanism by which electromagnetic radiation is
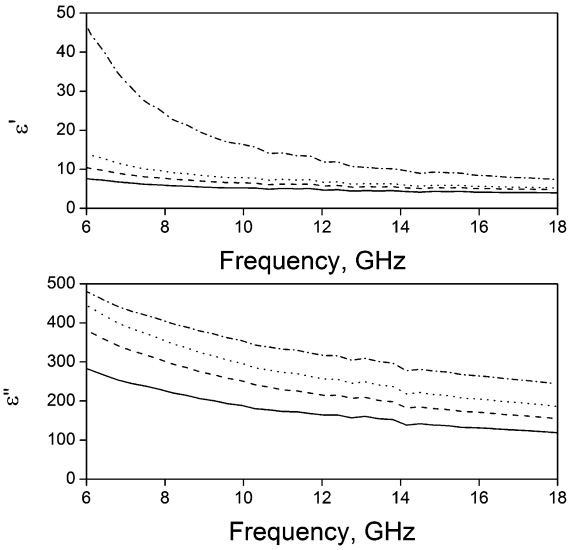
Fig. 5 Dielectric complex permittivity of the conductive walls: GR (solid), GR:CNT10% (dash), GR:CNT20% (dot), and GR:CNT40% (dash dot).
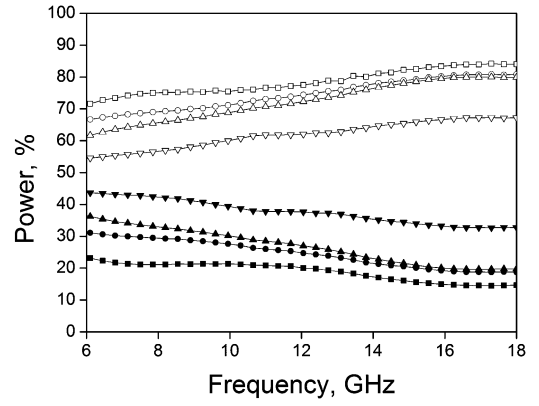

Fig. 6 Reflection coefficient of GR0% (■), GR:CNT10% (●), GR:CNT20% (▲), GR:CNT40% (▼) and the absorption coefficient of GR0% (□), GR:CNT10% (○), GR:CNT20% (△), and GR:CNT40% (▽). Specimens with thicknesses of 9 mm.

deactivated is essentially resistive. We can visualize this mechanism as a set of reflections of incident radiation on the walls of the pores where it becomes partially deactivated through the generation of electrical current in each impact.

Three mechanisms for electromagnetic shielding are commonly accepted: reflection, absorption and multiple reflections.[3] Multiple reflections are produced by the coupling of the reflected radiation on the first incident plane and reflection in the final plane of the material. This radiation coupling gives rise to constructive and destructive wave interferences that are frequency dependent. According to SchelKunoff's theory multiple reflections can be neglected when the thickness of the slab is greater than the skin depth (δ),[40,41] which is the depth at which the incident field decreases at $1/e$ of its initial value. We estimate that in samples with a slab thickness of about three times the skin depth, multiple reflections may become negligible (see the ESI†), and therefore, for our samples (9 mm thickness) this mechanism may become negligible for frequencies higher than 6 GHz.

Fig. 6 shows the reflected and absorbed power (P_R and P_A) of the GR–CNT composites measured in the 6–18 GHz frequency range. In all cases the transmitted power was particularly low, not exceeding in any case 5% of incident power (Fig. 6SI of the ESI†). Furthermore, the absorbed power was considerably greater than the power reflected by the material. These results indicate that all the measured systems can be considered as electromagnetic radiation absorbing materials. In our previous work,[4] we demonstrated that the larger the pore size, the greater the absorption power. This is due to an increase in the ratio between the pore size and the size of the conductive wall that should cause a lower impedance mismatch between air and the sample surface decreasing thus the reflected power.[42] The absorbed power is dependent on the power reflected; if the reflected power is very high the amount of radiation penetrating into the material is very small, and therefore the absorption will also be small. The reflected power

depends mainly on the impedance mismatch between the medium and the plane of incidence of the material. Thus, small changes in porosity within the plane of incidence also cause considerable changes in the reflected power and therefore also in the absorbed power. Samples containing higher CNTs are more reflective as a consequence of a higher electrical conductivity.[43–45] Therefore, the sample that only contains graphene presents the highest P_A which decreases as the CNT content is increased due to the higher amount of reflected power.

The electromagnetic shielding mechanism was investigated through a shielding efficiency (SE) analysis (eqn (2), (3) and (4)). Fig. 7 shows the SE due to the reflection and absorption for the hybrid composites. SE_R has negligible values in all the frequency range. SE_A, in contrast, increases with frequency for all samples, suggesting that absorption is the main electromagnetic dissipation mechanism.

Once the incident electromagnetic wave enters into the material, enhanced electrical conduction involves a better dissipation of energy across the samples. While comparing the effects of the CNT concentration, it is observed that SE_A (and SE_T, see the ESI†) increases with CNT content. Although this observation is consistent with previous reports about the electromagnetic
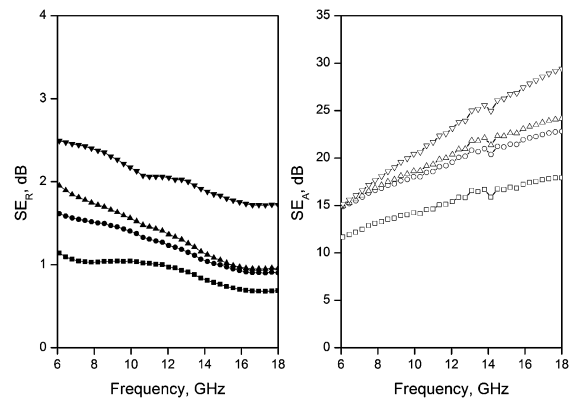

Fig. 7 Reflection (left) and absorption (right) shielding efficiency of GR0% (■), GR:CNT10% (●), GR:CNT20% (▲), and GR:CNT40% (▼).
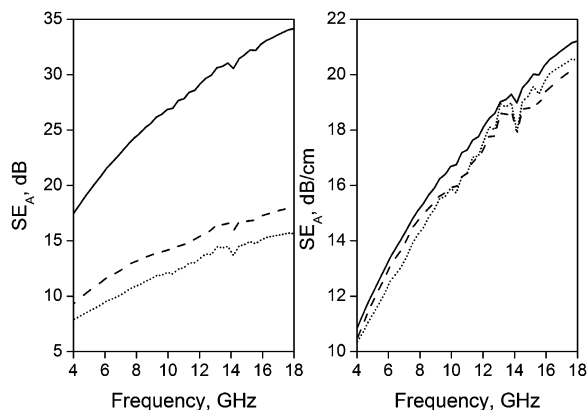
Fig. 8 Absorbed shielding efficiency (left) of GR scaffolds with composite thicknesses of: 16 mm (line), 9 mm (dash), and 6 mm (dots). Specific SE_A in dB cm^{-1} (right) as a representative set.

shielding of CNTs,[40] it may appear to be contradictory to the previous power analysis. However, it should be remarked that although high amounts of CNTs could absorb more radiation because of their high conductivity, radiation cannot penetrate due to reflection.

According to Al-Saleh *et al.*,[40] electromagnetic efficiency due to absorption is proportional to material thickness. Fig. 8 shows a comparative study of SE_A of graphene scaffold composites for three different thickness values (left) and the specific SE_A in dB cm^{-1} (right) as a representative set. Other compositions gave similar results. The three thicknesses appear to merge into a single curve although slight differences attributed to measurement errors and to slight differences in surface reflectivity can be observed. These results allow us to estimate the necessary thickness of a coating made by these methods to achieve optimal electromagnetic shielding for a specific application.

Conclusions

GR/CNT hybrid composites with controlled porosity *via* a modified hydrothermal method (HT) have been successfully prepared as electromagnetic shielding materials in the GHz range. We have taken advantage of the surface activity of GO platelets to stabilize large hexane droplets in a water suspension during the high temperature hydrothermal reduction. In this way we have been able to obtain a bimodal porous structure as revealed by SEM analysis: a microporous structure (10 microns) due to HT and a macroporous structure (250 microns) due to the hexane droplets.

Characterization by XRD, Raman, XPS and FTIR has shown a reduction process in GO after HT without affecting the reduction state of CNT. Fitting effective permittivity data to the Maxwell–Garnet model has allowed the extraction of relevant dielectric information on the conductive phase: as CNT content increases the dipolar polarization in the conductive phase also increases due to the Maxwell–Wagner–Sillars effect, and losses appear to level off for loadings higher than 20%. In all cases the transmitted power of the samples with a thickness of 9 mm was

particularly low, not exceeding in any case 5% of incident power. In all cases, the absorbed power was significantly greater (close to 80% of incident power) than the power reflected (close to 20% of incident power). These results as well as shielding efficiency analysis results allow us to affirm that all the studied systems can be considered as electromagnetic radiation absorbing materials.

Acknowledgements

References

1 S. Biswas, G. P. Kar and S. Bose, *Nanoscale*, 2015, **7**, 11334–11351.
2 K. Singh, A. Ohlan, V. H. Pham, R. Balasubramanian, S. Varshney, J. Jang, S. H. Hur, W. M. Choi, M. Kumar, S. K. Dhawan, B. S. Kong and J. S. Chung, *Nanoscale*, 2013, **5**, 2411–2420.
3 D. Chung, *Carbon*, 2001, **39**, 279–285.
4 M. González, M. Crespo, J. Baselga and J. Pozuelo, *Nanoscale*, 2016, **8**, 10724–10730.
5 D. R. Dreyer, S. Park, C. W. Bielawski and R. S. Ruoff, *Chem. Soc. Rev.*, 2010, **39**, 228–240.
6 L. Qiu, X. Yang, X. Gou, W. Yang and Z. F. Ma, *Chem. – Eur. J.*, 2010, **16**, 10653–10658.
7 F. Kim, L. J. Cote and J. Huang, *Adv. Mater.*, 2010, **22**, 1954–1958.
8 Z. Liu, J. T. Robinson, X. Sun and H. Dai, *J. Am. Chem. Soc.*, 2008, **130**, 10876–10877.
9 H. Yang, F. Li, C. Shan, D. Han, Q. Zhang, L. Niu and A. Ivaska, *J. Mater. Chem.*, 2009, **19**, 4632–4638.
10 Y. Xu, H. Bai, G. Lu, C. Li and G. Shi, *J. Am. Chem. Soc.*, 2008, **130**, 5856–5857.
11 L. Zhang, F. Zhang, X. Yang, G. Long, Y. Wu, T. Zhang, K. Leng, Y. Huang, Y. Ma, A. Yu and Y. Chen, *Sci. Rep.*, 2013, **3**, 1408.
12 Y. Xu, K. Sheng, C. Li and G. Shi, *ACS Nano*, 2010, **4**, 4324–4330.
13 H. Gao and H. Duan, *Biosens. Bioelectron.*, 2015, **65**, 404–419.
14 N. Cao and Y. Zhang, *J. Nanomater.*, 2015, 168125.
15 V. Mani, B. Devadas and S. M. Chen, *Biosens. Bioelectron.*, 2013, **41**, 309–315.
16 S. H. Lee, D. H. Lee, W. J. Lee and S. O. Kim, *Adv. Funct. Mater.*, 2011, **21**, 1338–1354.
17 Y. Zhu, L. Li, C. Zhang, G. Casillas, Z. Sun, Z. Yan, G. Ruan, Z. Peng, A. R. O. Raji, C. Kittrell, R. H. Hauge and J. M. Tour, *Nat. Commun.*, 2012, **3**, 1225.
18 V. Mani, S. M. Chen and B. S. Lou, *Int. J. Electrochem. Sci.*, 2013, **8**, 11641–11660.
19 Y. Li, J. Chen, L. Huang, C. Li, J. D. Hong and G. Shi, *Adv. Mater.*, 2014, **26**, 4789–4793.
20 L. Shahriary and A. Athawale, *Int. J. Renew. Energy Environ. Eng.*, 2014, **02**, 58–63.
21 O. Martín, H. R. Gutierrez, A. Maroto-Valiente, M. Terrones, T. Blanco and J. Baselga, *Mater. Chem. Phys.*, 2013, **140**, 499–507.

22 R. Lv, E. Cruz-Silva and M. Terrones, *ACS Nano*, 2014, **8**, 4061–4069.

23 Agilent, 85071E Materials Measurement Software.

24 M. Crespo, N. Méndez, M. González, J. Baselga and J. Pozuelo, *Carbon*, 2014, **74**, 63–72.

25 G. M. Kontogeorgis and S. Kiil, *Introduction to Apllied Colloid and Surface Chemistry*, Surface and Interfacial Tensions-Principles and Estimation Methods, Wiley, 2016, ch. 3, p. 71.

26 P. Guo, H. Song and X. Chen, *J. Mater. Chem.*, 2010, **20**, 4867.

27 H. Hu, Z. Zhao, W. Wan, Y. Gogotsi and J. Qiu, *Adv. Mater.*, 2013, **25**, 2219–2223.

28 J. W. Jang, S. Cho, G. H. Moon, K. Ihm, J. Y. Kim, D. H. Youn, S. Lee, Y. Lee, W. Choi, K. H. Lee and J. S. Lee, *Chem. – Eur. J.*, 2012, **18**, 2762–2767.

29 C. Wang, X. Han, P. Xu, X. Zhang, Y. Du, S. Hu, J. Wang and X. Wang, *Appl. Phys. Lett.*, 2011, **98**, 2011–2014.

30 N. Deprez and D. S. McLachlan, *J. Phys. D: Appl. Phys.*, 1988, **21**, 101–107.

31 Q. Liu, D. Zhang and T. Fan, *Appl. Phys. Lett.*, 2008, **93**, 013110.

32 L. W. Hrubesh, L. E. Keene and V. R. Latorre, *J. Mater. Res.*, 1993, **8**, 1736.

33 F. Moglie, D. Micheli, S. Laurenzi, M. Marchetti and V. Mariani Primiani, *Carbon*, 2012, **50**, 1972–1980.

34 Z. M. Dang, J. K. Yuan, S. H. Yao and R. J. Liao, *Adv. Mater.*, 2013, **25**, 6334–6336.

35 P. Xu, X. Han, C. Wang, D. Zhou, Z. Li, A. Wen, X. Wang and B. Zhang, *J. Phys. Chem. B*, 2008, **112**, 10443–10448.

36 H. Zhang, J. Zhang and H. Zhang, *Composites, Part A*, 2007, **38**, 602–608.

37 H. Zhang, J. Zhang and H. Zhang, *Comput. Mater. Sci.*, 2007, **38**, 857–864.

38 M. Hotta, M. Hayashi, M. T. Lanagan, D. K. Agrawal and K. Nagata, *ISIJ Int.*, 2011, **51**, 1766–1772.

39 J. G. Elton and E. Kaxiras, *Nano Lett.*, 2013, **13**, 898.

40 M. H. Al-Saleh and U. Sundararaj, *Carbon*, 2009, **47**, 1738–1746.

41 M. H Al-Saleh, W. H. Saadeh and U. Sundararaj, *Carbon*, 2013, **60**, 146–156.

42 N. Zhao, T. Zou, C. Shi, J. Li and W. Guo, *Mater. Sci. Eng., B*, 2006, **127**, 207–211.

43 B. Wen, X. X. Wang, W. Q. Cao, H. L. Shi, M. M. Lu, G. Wang, H. B. Jin, W. Z. Wang, J. Yuan and M. S. Cao, *Nanoscale*, 2014, **6**, 5754–5761.

44 T. K. Gupta, B. P. Singh, R. B. Mathur and S. R. Dhakate, *Nanoscale*, 2014, **5**, 842–851.

45 M. T. Chen, L. Zhang, S. S. Duan, S. L. Jing, H. Jiang, M. L. Luo and C. Z. Li, *Nanoscale*, 2014, **6**, 3796–3803.